

## SPITZER 70 $\mu$ m AND 160 $\mu$ m OBSERVATIONS OF THE EXTRAGALACTIC FIRST LOOK SURVEY

D. T. FRAYER<sup>1</sup>, D. FADDA<sup>1</sup>, L. YAN<sup>1</sup>, F. R. MARLEAU<sup>1</sup>, P. I. CHOI<sup>1</sup>, G. HELOU<sup>1</sup>, B. T. SOIFER<sup>1</sup>,  
P. N. APPLETON<sup>1</sup>, L. ARMUS<sup>1</sup>, R. BECK<sup>1</sup>, H. DOLE<sup>2</sup>, C. W. ENGELBRACHT<sup>3</sup>, F. FANG<sup>1</sup>, K. D.  
GORDON<sup>3</sup>, I. HEINRICHSEN<sup>1</sup>, D. HENDERSON<sup>1</sup>, T. HESSELROTH<sup>1</sup>, M. IM<sup>4</sup>, D. M. KELLY<sup>3</sup>, M.  
LACY<sup>1</sup>, S. LAINE<sup>1</sup>, W. B. LATTER<sup>1</sup>, W. MAHONEY<sup>1</sup>, D. MAKOVUZ<sup>1</sup>, F. J. MASI<sup>1</sup>, J. E.  
MORRISON<sup>3</sup>, M. MOSHIR<sup>1</sup>, A. NORIEGA-CRESPO<sup>1</sup>, D. L. PADGETT<sup>1</sup>, M. PESENSON<sup>1</sup>, D. L.  
SHUPE<sup>1</sup>, G. K. SQUIRES<sup>1</sup>, L. J. STORRIE-LOMBARDI<sup>1</sup>, J. A. SURACE<sup>1</sup>, H. I. TEPLITZ<sup>1</sup>, G. WILSON<sup>1</sup>

Accepted AJ, 2005 Sep 21

### ABSTRACT

We present *Spitzer* 70 $\mu$ m and 160 $\mu$ m observations of the *Spitzer* extragalactic First Look Survey (xFLS). The data reduction techniques and the methods for producing co-added mosaics and source catalogs are discussed. Currently, 26% of the 70 $\mu$ m sample and 49% of the 160 $\mu$ m-selected sources have redshifts. The majority of sources with redshifts are star-forming galaxies at  $z < 0.5$ , while about 5% have infrared colors consistent with AGN. The observed infrared colors agree with the spectral energy distribution (SEDs) of local galaxies previously determined from *IRAS* and *ISO* data. The average 160 $\mu$ m/70 $\mu$ m color temperature for the dust is  $T_d \simeq 30 \pm 5$  K, and the average 70 $\mu$ m/24 $\mu$ m spectral index is  $\alpha \simeq 2.4 \pm 0.4$ . The observed infrared to radio correlation varies with redshift as expected out to  $z \sim 1$  based on the SEDs of local galaxies. The xFLS number counts at 70 $\mu$ m and 160 $\mu$ m are consistent within uncertainties with the models of galaxy evolution, but there are indications that the current models may require slight modifications. Deeper 70 $\mu$ m observations are needed to constrain the models, and redshifts for the faint sources are required to measure the evolution of the infrared luminosity function.

*Subject headings:* galaxies: evolution — galaxies: starburst — infrared: galaxies

### 1. INTRODUCTION

One of the first science observations carried out with the *Spitzer Space Telescope* (Werner et al. 2004) was the non-proprietary extragalactic First Look Survey (xFLS) which was designed to characterize the infrared sky at previously unexplored sensitivities. The *IRAS* mission first uncovered the presence of infrared luminous galaxies in the local universe (Neugebauer et al. 1984; Soifer et al. 1987), and the *ISO* infrared (Elbaz et al. 1999, 2002; Rodighiero et al. 2005) and ground-based submillimeter and millimeter observations (Blain et al. 2002 and references therein) have highlighted the importance that infrared luminous galaxies have on the general understanding of galaxy evolution. Since the cosmic infrared background (CIB) peaks in the far-infrared (FIR) (Hauser & Dwek 2001), studying the properties of galaxies that are bright in the FIR is crucial for constraining models of galaxy evolution.

In this paper, we present 70 $\mu$ m and 160 $\mu$ m observations of the xFLS field using the Multiband Imaging Photometer for *Spitzer* (MIPS, Rieke et al. 2004). The xFLS is a 4 deg<sup>2</sup> survey. The SWIRE *Spitzer* survey (Lonsdale et al. 2004) covers a wider area (49 deg<sup>2</sup>) to similar depths, and deeper observations covering smaller areas are being taken by the MIPS Instrument Team as part of the Guaranteed Time Observers (GTO) program (e.g., Dole et al. 2004a) and other groups. Although the xFLS is not unique in terms

of depth or area coverage, the field has a large number ( $\sim 3000$ ) of spectroscopic redshifts (P. Choi et al. 2005, in preparation; F. Marleau et al. 2005, in preparation), ancillary radio (Condon et al. 2003), and optical imaging data (Fadda et al. 2004) that permit detailed multi-wavelength studies over a relatively large area. In this paper, we measure the source counts and use the available redshifts to constrain the rest-frame spectral energy distributions (SEDs) and derive the average infrared properties for the xFLS 70 $\mu$ m and 160 $\mu$ m populations. A cosmology of  $H_0 = 70$  km s<sup>-1</sup> Mpc<sup>-1</sup>,  $\Omega_M = 0.3$ , and  $\Omega_\Lambda = 0.7$  is assumed throughout this paper.

### 2. OBSERVATIONS

The xFLS survey covers a 4 deg<sup>2</sup> region (17<sup>h</sup>18<sup>m</sup>00<sup>s</sup>, +59°30'00'') within the northern continuous viewing zone of *Spitzer*<sup>5</sup>. Inside the xFLS main field a smaller verification strip of 0.25 deg<sup>2</sup> centered at 17<sup>h</sup>17<sup>m</sup>00<sup>s</sup>, +59°45'00'' was observed with an integration time of 4 times that of the main survey to characterize the completeness and source reliability of the main survey. In total, 27.7 hours of xFLS observations were taken in 2003 December with the MIPS instrument. An additional 16.8 hours of observations within the xFLS main field were taken in 2005 May to characterize the performance of the 70 $\mu$ m array at warmer telescope temperatures ( $T_{mirror} \simeq 9.5$  K). These observations produced useful data at 70 $\mu$ m, but the 160 $\mu$ m

<sup>1</sup>*Spitzer* Science Center, California Institute of Technology 220–06, Pasadena, CA 91125; frayer@ipac.caltech.edu.

<sup>2</sup>Institut d' Astrophysique Spatiale, bât 121, Université Paris Sud, F-91405 Orsay Cedex, France.

<sup>3</sup>Steward Observatory, University of Arizona, 933 North Cherry Avenue, Tucson, AZ 85721.

<sup>4</sup>Astronomy Program, Seoul National University, Shillim-dong, Kwanak-gu, Seoul, S. Korea, 2-880-9010.

<sup>5</sup>The extragalactic FLS data can be retrieved from the *Spitzer* Science Center at <http://ssc.spitzer.caltech.edu/fls/>

data were not usable. Figure 1 shows the layout of the observations.

All of the MIPS observations were taken using the medium scan-rate mapping mode (4.2s data collection events [DCEs]). The main-survey data were taken with adjacent 2 deg scan legs that were offset in the cross-scan direction by 276'' (nearly the full field of view of the arrays). The main-survey was covered twice to identify potential asteroids and to increase the redundancy of the data set. Unfortunately, half of the MIPS-70 array was rendered useless after launch due to a cable failure outside the instrument (Rieke et al. 2004). Therefore, at 70 $\mu$ m each position of the main survey was covered by only one scan leg. Since the data were not scheduled exactly as originally planned, slight rotations between the 8 astronomical observation requests (AORs) yielded small gaps with zero coverage in the south-west corner of the main-survey 70 $\mu$ m map.

The verification strip was observed using 4 AORs with 0.5 deg scan legs at the medium scan rate. Each AOR covered the 0.5 deg $\times$ 0.5 deg field using cross-scan steps of 148'' (slightly less than half an array field of view). The warm test data taken in 2005 May were centered on the 70 $\mu$ m main-field. These data consisted of 6 AORs with 1.75 deg scan legs. Cross-scan steps of 148'' were used to map the 1.75 deg $\times$ 1.75 deg field once. Table 1 shows the average integration times, sensitivities, and area coverage for the 70 $\mu$ m and 160 $\mu$ m observations.

### 3. DATA REDUCTION

#### 3.1. BCD Pipeline Processing

The raw 70 $\mu$ m and 160 $\mu$ m (MIPS-Germanium [Ge]) data were downloaded from the *Spitzer* Science Center (SSC) archive and were reduced using the offline Ge Reprocessing Tools (GeRT), available from the public SSC website. The GeRT uses an offline version of the SSC pipeline to produce the basic calibrated data products (BCDs), following the algorithms derived by the MIPS Instrument Team and the MIPS Instrument Support Team (Gordon et al. 2005). The processing was done using the latest software (SSC pipeline version S12) to take advantage of improvements not currently available for the online xFLS data products (made with pipeline version S11).

BCD processing has two main steps: (1) calculation of the slope of the data ramp, and (2) calibration of the slope image. For the xFLS MIPS-Ge data, the raw 4.2s data ramps are comprised of 32 non-destructive reads per pixel (one DCE). After correcting for the electronic nonlinearity, cosmic ray events and other discontinuities are identified in the data ramps. The SSC pipeline identifies discontinuities using a maximum likelihood technique (Hesselroth et al. 2000). Linear slopes are calculated for the ramp segments between discontinuities and checked for consistency. The slopes from the segments are combined based on the empirical errors estimated from the scatter of the data within the ramp segments. Average slopes for each pixel are calculated to produce an uncalibrated slope image.

The second step of BCD processing is the calibration of the slope image. The calibration of MIPS-Ge data is based on frequent measurements of internal stimulator flashes

(stims) which are used to track the responsivity of the detectors as a function of time. For the xFLS medium scan-rate data, the stim flashes are observed every 25 DCEs (118s). The stim flash signal is measured by subtracting the previous “background” DCE from the stim frame which is taken at the same position on the sky. For each AOR, a stim response function ( $SR[t]$ ) is calculated from interpolating between the stim minus background measurements.

After the determination of the stim response as a function of time ( $SR[t]$ ), the BCD data are calibrated using the following equation:

$$BCD(t) = FC[U(t)/SR(t) - DARK]/IC, \quad (1)$$

where  $U(t)$  is the uncalibrated slope image, DARK is the dark calibration file, and IC is the illumination correction calibration file which corrects for the combined illumination pattern from the telescope and the stim flash signal. The DARK and IC calibration files are stable and are generated by combining data from several different campaigns to improve the signal-to-noise. The flux conversion factor ( $FC$ ) converts the instrument units into physical surface brightness units of MJy sr $^{-1}$  and is derived from observations of standard calibrators (Sec. 3.4).

#### 3.2. BCD Filtering

Before the 70 $\mu$ m bias level was lowered in 2004 March, the 70 $\mu$ m data showed significant data artifacts. Examples and discussion of MIPS-Ge artifacts are shown in the MIPS Data Handbook<sup>6</sup>. The two main artifacts impacting the xFLS data are the stim flash latents and the variations of the slow response as a function of time. The 160 $\mu$ m data are affected by these issues to a lesser degree due to the faster time constants of the 160 $\mu$ m stressed-Germanium detectors. For point sources, the stim latent and slow response residuals are additive effects. The filtering of the 160 $\mu$ m data is straight-forward. We used the filtered BCDs products, which remove a running median per pixel as a function of time by subtracting the median value for the surrounding DCEs closest in time (ignoring the current DCE, stim DCEs, and bad data). This high-pass time median filter removes data artifacts as well as the extended cirrus emission. To remove the stim latent artifacts at 160 $\mu$ m, we simply ignored the first DCE after the stim flash since the stim latents decay away within one DCE.

The filtering process for the 70 $\mu$ m data is slightly more complicated. The time median filter by itself does not remove all of the data artifacts. Stim latents remain for many DCEs and are correlated by column. Since the scan map direction is nearly along the columns of the array (along the y-axis), the column artifacts are amplified. We remove the column residuals by subtracting the median of the values along each column for every BCD. The combination of the high-pass time median filter per pixel and the column median filter removes the bulk of the data artifacts at 70 $\mu$ m.

The resultant rms is lower for narrow high-pass median filter widths (< 15 DCEs), but narrow filter windows can yield significant negative side-lobes around bright sources.

<sup>6</sup><http://ssc.spitzer.caltech.edu/mips/dh/>

In addition, column filtering does not maintain point source calibration for the brightest sources ( $\gtrsim 0.5$  Jy). To avoid significant negative side-lobes and to preserve calibration, the filtering of the MIPS-Ge data was done in two passes. The data from the first filtering pass were co-added, and sources were extracted (Sec. 3.3) to find the location of the bright sources. The source positions within the original BCDs were masked and new filtering corrections were calculated in the second pass, ignoring the pixels containing sources. This second-pass filtering technique minimizes the data artifacts while preserving point-source calibration.

Different filtering methods were tested and optimized using the GeRT. At  $70\mu\text{m}$ , we applied column filtering followed by a high-pass time median filter with a width of 12 DCEs to yield the deepest image. The final sensitivity of the filtered  $70\mu\text{m}$  image was improved by more than a factor of two in comparison to data with no filtering. Filtering has less of an impact at  $160\mu\text{m}$ , but is useful for deep observations of faint point sources. We adopted a high-pass time median filter width of 12 DCEs for the  $160\mu\text{m}$  data using the second-pass filtering technique as done for  $70\mu\text{m}$ .

### 3.3. Data Coaddition and Source Extraction

The filtered BCDs were coadded using the SSC mosaicing and source extraction software (MOPEX) (Makovoz & Marleau 2005). The data were combined ignoring bad data flagged in the BCD mask files (bmask) and the bad pixels defined by the static pixel mask (pmask). Using the redundancy of the MIPS data, additional spurious data values were removed via outlier rejection. The remaining data were corrected for array distortions and projected onto a sky grid with square pixels that were more than 2 times smaller than the original pixels. The output mosaic pixels are  $4''$  at  $70\mu\text{m}$  and  $8''$  at  $160\mu\text{m}$ . The data were averaged using weights proportional to the fractional area subtended by the original pixels as projected onto the output pixel grid. Since the calibration of the main, verification, and the warm  $70\mu\text{m}$  data sets are consistent within measurement errors, all data were combined to yield the deepest images.

Sources were extracted from the final images using MOPEX. The MOPEX software uses a Point-source Response Function (PRF) image to optimize source detection and point source fitting. A PRF calibration image was made for each MIPS band by coadding isolated bright point sources within the xFLS field. A point source probability (PSP) image was made from non-linear matched filtering of the input image with the PRF. The PSP image represents the probability of having a point source above the noise at each pixel. The PSP image was multiplied by the input image to yield the filtered image used for source detection. The filtered image enhances the presence of point sources in the mosaic while smoothing out noise features that do not match the input PRF, providing a more robust image for source detection. After source detection, the original images were fitted with the PRF image via  $\chi^2$  minimization to extract source positions and flux densities. Regions containing multiple peaks were de-blended. For extended sources and/or close blends, not well fitted

by the PRF, large aperture measurements were used to derive the total flux density for the source.

The noise across the images is non-uniform. For optimal source detection and extraction, an accurate representation of the uncertainties is needed. The MOPEX uncertainty image based on the input BCD pipeline uncertainties is useful for identifying the relative uncertainties across the image, but the pipeline errors typically underestimate the absolute uncertainty level for low background regions. The median level of the MOPEX uncertainty image was scaled to match the average empirical noise in the mosaics. By using a properly scaled uncertainty image, we find an average  $\chi^2$  for the fitted point sources of  $\chi^2 \simeq 1$ , suggesting that the uncertainty image is self-consistent with the average point source errors in the data.

Several tests were done to validate the photometric results from MOPEX. No calibration differences were found for different sub-sets of the data. We also compared the photometry done with the MOPEX software with that from the program StarFinder (Diolaiti et al. 2000). Both programs use an empirical PRF to fit source flux density. The results from MOPEX and StarFinder agree to better than 5% for bright point sources ( $\gtrsim 50$  mJy at  $70\mu\text{m}$  and  $\gtrsim 200$  mJy at  $160\mu\text{m}$ ) and better than 10% rms down to the limits of the catalog, consistent with the uncertainties in the data. For faint sources detected in the MIPS-Ge bands, PRF fitting techniques yield more reliable results than aperture measurements. By comparing results between the verification data and the main survey, we find a consistency of  $\pm 10\%$  for PRF matching techniques and a dispersion for aperture measurements of larger than  $\pm 25\%$  at faint flux density levels.

### 3.4. Calibration

The absolute calibration is derived using observations of stars at  $70\mu\text{m}$  and observations of asteroids and well-studied luminous infrared galaxies at  $160\mu\text{m}$ . The data were processed assuming flux conversion factors of  $634$  MJy sr $^{-1}$  per MIPS-70 data unit and  $42$  MJy sr $^{-1}$  per MIPS-160 data unit. The flux densities in the source catalogs were multiplied by the correction factors of 1.16 and 1.17 for the MIPS-70 and MIPS-160 bands respectively, which includes the color corrections associated with a constant  $\nu f_\nu$  SED and updated calibration conversion factors based on the latest measurements. Additional color corrections for sources with non-constant  $\nu f_\nu$  SEDs are negligible since the color corrections are similar for the range of SEDs appropriate for galaxies;  $f_\nu \propto \nu^{-\alpha}$ , where  $\alpha \sim 0-3$ . For flux density ranges of  $50$  mJy– $2$  Jy, the absolute calibration uncertainty is estimated to be about 15% and 25% for the  $70\mu\text{m}$  and  $160\mu\text{m}$  bands respectively. No corrections have been made for possible flux nonlinearities, which may be significant for sources brighter than this nominal flux density range. Observers are recommended to check the latest information on MIPS calibration at the SSC web site.

We confirmed that the absolute  $70\mu\text{m}$  flux density scale for the xFLS data is consistent with previous measurements made by *IRAS* to within 10%. For comparison with *IRAS*, we interpolated between the flux densities in *IRAS*-60 and *IRAS*-100 bands (Beichman et al. 1988) to the ef-

<sup>7</sup>The effective wavelengths of the MIPS-24, 70, and 160 bands are  $23.7\mu\text{m}$ ,  $71.4\mu\text{m}$ , and  $155.9\mu\text{m}$ , respectively. Throughout this paper, the

fective wavelength of the MIPS-70 band ( $71.4\mu\text{m}$ )<sup>7</sup> applying the appropriate color corrections. For the five brightest sources in the field detected by *IRAS*, we derive a flux density ratio of  $Spitzer/IRAS = 1.0 \pm 0.1$  at  $71.4\mu\text{m}$ . The calibration at  $160\mu\text{m}$  is more uncertain given that xFLS sources have not been observed previously at wavelengths longer than  $100\mu\text{m}$ . Simple SED model fits to the data indicate that the calibration at  $160\mu\text{m}$  is consistent with *IRAS* to within 30%.

### 3.5. Mosaics and Catalogs

The MIPS-Ge mosaics and catalogs are available online at the SSC website. For both of the MIPS-70 and  $160\mu\text{m}$  bands, we provide coadded mosaics of the entire xFLS data sets along with the corresponding coverage maps and uncertainty images. The mosaics are from the filtered products and have been background subtracted. The absolute level of the uncertainty image has been scaled to match the empirical noise within the mosaics. The coverage map represents the effective number of input BCDs for each pixel of the mosaic after outlier rejection. There are regions within the  $70\mu\text{m}$  and  $160\mu\text{m}$  mosaics with zero coverage. The  $70\mu\text{m}$  image has gaps in the south-west corner of the mosaic due to non-overlapping AORs. The  $160\mu\text{m}$  mosaics have a regular pattern of low coverage due to the unusable block of five detectors and the low redundancy of these observations.

Point-source catalogs were made for sources with  $S/N > 7$  at each wavelength to insure high reliability. Sources near the edges or within regions of very low coverage were deleted from the public catalogs to avoid potentially spurious sources. In total, 687  $70\mu\text{m}$  sources (Table 2) and 207  $160\mu\text{m}$  sources (Table 3) are cataloged. The  $70\mu\text{m}$  and  $160\mu\text{m}$  catalogs are independent. The catalogs can be combined together or with xFLS data at other wavelengths, depending on the specific application. The average point source rms ( $1\sigma$ ) is 2.8 mJy and 20 mJy for the  $70\mu\text{m}$  warm+main data and  $160\mu\text{m}$  main-survey data, respectively. For the deeper verification regions, the point source rms is 1.6 mJy at  $70\mu\text{m}$  and 10 mJy at  $160\mu\text{m}$ .

The images were examined visually to validate source detection and to determine the appropriate method for deriving the flux densities on a source by source basis. About 98% of the derived flux densities are based on PRF fitting (Sec. 3.3). The remaining sources mostly consist of bright extended galaxies and/or close blends that are not well fitted by the PRF. In these cases, large aperture measurements were made to derive the total flux densities. For bright extended sources that have one or more neighboring point sources within the aperture, the flux density of the bright galaxy was derived by subtracting the PRF measurement(s) of the faint point source(s) from the total aperture measurement.

Table 2&3 show the format for an example portion of the xFLS MIPS  $70\mu\text{m}$  and  $160\mu\text{m}$  catalogs published in the online edition of the Journal. The average radial positional errors are  $2''.6$  and  $5''.2$  ( $1\sigma$ ) for the  $S/N > 7$  MIPS-70 and  $160\mu\text{m}$  sources respectively. No systematic differences are found for the  $70\mu\text{m}$  source coordinates ( $< 0''.2$ ) in comparison to the more accurate  $24\mu\text{m}$  positions. For consistency with the  $24\mu\text{m}$  and  $70\mu\text{m}$  data, we correct the  $160\mu\text{m}$  position flux densities for the MIPS-bands are defined as  $S_{24} \equiv S_{\nu}(23.7\mu\text{m})$ ,  $S_{70} \equiv S_{\nu}(71.4\mu\text{m})$ , and  $S_{160} \equiv S_{\nu}(155.9\mu\text{m})$ .

sitions by  $4''.7$  to compensate for the systematic positional offset measured for the  $160\mu\text{m}$  sources (a known issue for pre-S12 versions of the pointing pipeline). The flux densities have been color corrected assuming a constant  $\nu f_{\nu}$  SED. The tabulated flux density errors include the absolute flux density uncertainties of 15% and 25% at  $70\mu\text{m}$  and  $160\mu\text{m}$ , respectively.

### 3.6. Reliability and Completeness

The verification data were used to test the reliability of the source detection and extraction techniques. For a high level of reliability at  $S/N < 10$ , it is important that the uncertainty image accurately reflects the small-scale spatial variations in the noise across the images. Using the uncertainties based on the BCDs, properly scaled to represent the average empirical noise in the data (Sec. 3.3), we obtained good results. Based on the deeper verification data, we do not find spurious sources with  $S/N > 5$  in the main survey within the verification field. Sources detected at  $S/N > 4$  are 80-85% reliable, and detections at the  $S/N > 3$  level are only 50-60% reliable. Based on these results, we adopted a  $S/N > 5$  cut for deriving the source counts in Sec. 4.1. A more conservative  $S/N > 7$  criterion was adopted for the public catalogs (Sec. 3.5).

At  $70\mu\text{m}$  the completeness and source counts were measured within the overlapping region of the warm and main fields (Fig. 1), while the entire main-field xFLS area was used at  $160\mu\text{m}$ . Both empirical completeness estimates based on the verification data and simulated completeness measurements were made. The simulations of completeness were carried out by adding point sources with different flux densities into the mosaics at random locations, and then extracting sources using the same techniques adopted for the source catalogs. The simulations and empirical methods for estimating completeness gave consistent results. Using the adopted  $S/N > 5$  criterion, the completeness level falls rapidly below 60% for  $S_{70} < 14\text{mJy}$  (Fig. 2) and  $S_{160} < 100\text{mJy}$  (Fig. 3). Similar completeness simulations were done for the deeper verification field, and we find 60% completeness levels of approximately 9 mJy and 60 mJy at  $70\mu\text{m}$  and  $160\mu\text{m}$ , respectively.

## 4. RESULTS AND DISCUSSION

### 4.1. Source Counts

The source counts are derived for the main xFLS and verification fields based on  $S/N > 5$  catalogs corrected for completeness. At  $70\mu\text{m}$  we use the  $3.3\text{ deg}^2$  region containing both the main and warm survey data. The  $160\mu\text{m}$  counts are based on the entire  $4.5\text{ deg}^2$  area of the main survey. Figures 4&5 show the differential source counts ( $dN/dS \times S^{2.5}$ ) at  $70\mu\text{m}$  and  $160\mu\text{m}$  respectively. Over the entire observed range of flux density, both the  $70\mu\text{m}$  and  $160\mu\text{m}$  counts increase at super-Euclidean rates with decreasing flux density.

In total 845 sources at  $70\mu\text{m}$  were detected ( $> 5\sigma$  at  $S_{70} < 440\text{mJy}$ ) within the main+warm field area and 186 sources were detected ( $S_{70} < 70\text{mJy}$ ) within the verification field (Table 4). In comparison at  $160\mu\text{m}$ , 227 sources were detected in the main-field ( $S_{160} < 880\text{mJy}$ ) and 45 sources ( $S_{160} < 140\text{mJy}$ ) were found in the verification field (Table 5). The source counts are consistent between

the main and verification data for the overlapping range of flux densities. The xFLS counts are also consistent within errors with the previous MIPS-Ge counts published by Dole et al. (2004a). The error bars for the source counts include the Poisson noise, the completeness errors, and the absolute flux density calibration uncertainty. The data were binned such that the errors are not dominated by Poisson statistics, except for the highest flux density bins. In the lowest flux density bins, the errors on completeness dominate the uncertainties.

Dole et al. (2004a) found a difference in the  $70\mu\text{m}$  counts between the CDF-S and Marano observations, which they attributed to field variations. The measured  $70\mu\text{m}$  xFLS counts are within the range of values previously measured, and closer to the CDF-S counts at faint flux densities. The xFLS-Ge counts are also consistent within uncertainties with the evolutionary models of Lagache et al. (2004), which were updated to match the *Spitzer*  $24\mu\text{m}$  counts. However, the xFLS data points are systematically slightly lower than the predictions from current models. Counts from the wide-area SWIRE survey would be needed to check for possible field variations and to test whether the models require slight modifications.

Although the xFLS  $70\mu\text{m}$  counts are at fainter levels than those previously published (Dole et al. 2004a), they are not yet deep enough to measure the location of the expected turn over of the differential counts (Fig. 4). The flux density at which the differential counts turn over provides important constraints on evolutionary models (Lagache et al. 2004; Chary & Elbaz 2001; King & Rowan-Robinson 2003; Xu et al. 2001), as shown by the  $24\mu\text{m}$  data (Marleau et al. 2004; Papovich et al. 2004; Chary et al. 2004). At  $160\mu\text{m}$  *Spitzer* is not expected to measure the turn over in the counts (Fig. 5), since the  $160\mu\text{m}$  data are expected to be limited by confusion below 40 mJy (Dole et al. 2004b). The differential counts at  $70\mu\text{m}$  are expected to turn over at around 10 mJy (Lagache et al. 2004), which is well above the confusion limit, suggesting that deeper  $70\mu\text{m}$  counts would provide useful constraints for galaxy evolution models.

#### 4.2. Infrared Colors

For high reliability, the source counts were derived using a  $S/N > 5$  criterion for the individual bands. However, it is possible to maintain a high level of reliability at lower  $S/N$  by using the MIPS- $24\mu\text{m}$  and/or radio data of the field. For studying the infrared colors, we used  $S/N > 4$  source lists to increase the number of sources detected at high-redshift in the MIPS-Ge bands. The  $70\mu\text{m}$  source list was bandmerged with the  $24\mu\text{m}$  catalog (D. Fadda et al., in preparation). At  $S/N > 4$ , 1779 xFLS-70 sources have counterparts at  $24\mu\text{m}$  within  $6''$ . The different resolutions of the  $24\mu\text{m}$ ,  $70\mu\text{m}$ , and  $160\mu\text{m}$  data sets ( $6''$ ,  $18''.5$ , and  $40''$ , respectively) complicate the identification of the counterparts in the MIPS bands. Out of the 1779  $70\mu\text{m}$  sources, 9% have multiple candidate  $24\mu\text{m}$  counterparts. To avoid potential spurious matches, we only used sources with one-to-one matches for studying the infrared colors. The  $4\sigma$  xFLS-160 source list was matched to the  $70\mu\text{m}$  data set using a positional matching radius of  $13''$ . The resulting matched MIPS-160+70 source list was matched

to the MIPS-70+24 source list. We find 301  $160\mu\text{m}$  sources with one-to-one matches between all three MIPS-bands.

Out of the 1618 xFLS-70 sources with one  $24\mu\text{m}$  positional match, 427 currently have redshifts. Approximately 57% of these sources come from the NOAO WIYN-Hydra radio-selected redshift survey (F. Marleau et al. in preparation), 16% of the redshifts are from the Keck-DEIMOS  $24\mu\text{m}$ -selected sample (P. Choi et al., in preparation), and the remaining 27% of redshifts are from the SLOAN survey (Strauss et al. 2002). The largest redshift to date is for a quasar at  $z = 3.56$ . For the  $160\mu\text{m}$ -selected sources with detections in all three MIPS-bands, about half (146) have known redshifts. Although the redshift survey of xFLS-Ge sources is not nearly complete (only 26% of the  $70\mu\text{m}$  sources and 49% of the  $160\mu\text{m}$  sources currently have redshifts), there are a sufficient number of sources to study the general trends in the infrared colors as a function of redshift for the sample.

We adopt two sets of SED models for studying the infrared colors. The first set of SED models is based on a simple modified blackbody (Blain, Barnard, & Chapman 2003). The SED is expressed as  $f_\nu = \epsilon_\nu B_\nu$ , where  $B_\nu(T_d, \nu)$  is the blackbody function for a dust temperature  $T_d$ , and  $\epsilon_\nu \propto \nu^\beta$  is the dust emissivity. In the mid-IR, we substitute a power-law of the form  $f_\nu \propto \nu^{-\alpha}$ , smoothly matching  $\epsilon_\nu B_\nu$  at longer wavelengths (Blain et al. 2003). For this simple SED model, there are three free parameters:  $T_d$ ,  $\beta$ , and  $\alpha$ . The S160/S70 ratio constrains  $T_d$ , while the S70/S24 ratio measures  $\alpha$ . The dust emissivity index  $\beta$  is not very well constrained by the *Spitzer* data alone. For simplicity, we adopt a constant value of  $\beta = 1.5$  which is consistent with the results for low-redshift *IRAS* galaxies (Dunne et al. 2000).

The second set of SED models uses a physically more realistic approach by assuming a power-law distribution of dust masses as a function of radiation field intensity (Dale et al. 2001). The dust mass ( $M_d$ ) as a function of the radiation field ( $U$ ) is given by  $dM_d(U) \propto U^{-\gamma} dU$  (Dale et al. 2001; Dale & Helou 2002)<sup>8</sup>. Quiescent, cirrus-like dust regions are expected to have  $\gamma \simeq 2.5$ , while environments near active HII regions are expected to be approximated by  $\gamma \simeq 1$ . For a mixture of active and quiescent regions, the average effective  $\gamma$  of star-forming galaxies should be between  $1 \lesssim \gamma \lesssim 2.5$ .

Figure 6 shows the observed  $70\mu\text{m}/24\mu\text{m}$  flux density ratio (S70/S24) plotted as a function of redshift with several predictions based on the SEDs of local galaxies. The majority of the xFLS sources have S70/S24 ratios within the range of values between the extreme ultraluminous starburst of Arp 200 and the more typical starburst M82. At moderate and high redshifts, infrared-cool ultraluminous infrared galaxies (ULIRGs,  $L > 10^{12} L_\odot$ ), e.g., Arp 220, are expected to have the highest S70/S24 ratios, while warm-infrared ULIRGs, e.g., Mrk 231, and AGN dominated sources are expected to have lower S70/S24 ratios. Spiral galaxies without a strong infrared excess in their SED (e.g., M100) show decreasing S70/S24 ratios as a function of redshift; however, these galaxies are not detected at high redshifts ( $z > 0.5$ ) in the xFLS-Ge survey. In general, the S70/S24 ratio can be used to help distinguish between AGN-dominated sources from star-forming

<sup>8</sup>We use  $\gamma$  to represent the “ $\alpha$ ” parameter of Dale et al. (2001).

galaxies, except in cases for which strong polycyclic aromatic hydrocarbon (PAH) emission features are redshifted into the  $24\mu\text{m}$  band (e.g., M82 at  $z \sim 2$  in Fig. 6) and for AGN with strong silicate absorption features (e.g., Spoon et al. 2004) at  $z \sim 1.5$ .

For the xFLS sample currently with redshifts, only 5% show low  $S70/S24$  ratios consistent with AGN SEDs. The AGN population is fitted with  $T_d = 90 \pm 30\text{K}$  and  $\alpha = 1.1 \pm 0.3$  (Fig. 6), which is consistent with the *IRAS* observations of Seyfert galaxies (Miley, Neugebauer, & Soifer 1985). The majority of the xFLS sample with redshifts are starbursts at  $z < 0.5$ . Figure 6 shows a large concentration of sources at  $z \sim 0.2$ . The  $S70/S24$  ratios based on the SEDs of quiescent and active galaxies (Dale & Helou 2002) intersect at  $z \sim 0.2$ , which may contribute to this concentration of data points. For the galaxies with  $z \simeq 0.2$ , the average observed infrared color is  $S70/S24 = 14 \pm 5$ . In comparison with the *IRAS* population (Soifer et al. 1989; Sanders et al. 2003), the *IRAS-60/IRAS-25* ratios correspond to a predicted ratio of  $S70/S24 = 14 \pm 3$ , consistent with the measured xFLS infrared colors. For the simple SED model, the average  $S70/S24$  ratio corresponds to an infrared index of  $\alpha = 2.4$ . Using SEDs of Dale & Helou (2002), values of  $\gamma \sim 2$  give the best agreement with the average  $S70/S24$  ratios.

Although the majority of the  $70\mu\text{m}$  sources do not have redshifts, the distribution of the  $S70/S24$  ratios is the same for galaxies with and without redshifts (Fig. 7). The average mid-IR spectral index is  $\alpha = 2.4 \pm 0.4$ . For a simple power-law representation of the mid-IR SED, the modeled  $S70/S24$  ratio is constant with redshift (e.g., Starburst solid line in Fig. 6). However, galaxies are expected to show significant variations in the  $S70/S24$  ratio as strong PAH emission and mid-IR absorption features (e.g., Armus et al. 2004) are redshifted through the  $24\mu\text{m}$  band (as seen for Arp 220 in Fig. 6).

Using simple modified blackbody SEDs, we calculate  $S160/S70$  as a function of redshift and dust temperature for a constant value of  $\alpha = 2.4$  (Fig. 8). The average  $160\mu\text{m}/70\mu\text{m}$  color temperature for the dust temperature is  $30 \pm 5\text{K}$ . This temperature is slightly lower than the average temperature of  $T_d = 38 \pm 3\text{K}$  (Dunne et al. 2000) and  $T_d \simeq 35\text{--}40\text{K}$  (Soifer et al. 1989) derived for *IRAS* galaxies, but the longer wavelength  $160\mu\text{m}$  band is more sensitive to regions with cooler dust temperatures than those observed by *IRAS*. The blackbody temperature of  $30\text{K}$  derived here agrees well with the long-wavelength *ISO* observations of infrared-bright spiral galaxies (Bendo et al. 2003). Bendo et al. (2003) found that  $T_d \simeq 30\text{K}$  provided the best fit to the *ISO* data for  $\beta \sim 1\text{--}2$ , consistent with the results in Figure 8. In the context of the SED models of Dale & Helou (2002), values of  $\gamma \sim 2\text{--}2.5$  provide the best agreement with the observed  $S160/S70$  ratios.

The distribution of the  $S160/S70$  ratios is measurably different for sources with and without redshifts (Fig. 9). Unlike the  $S70/S24$  ratio which is on average roughly constant with redshift, the  $S160/S70$  ratio is expected to increase with redshift (Fig. 8). Figure 9 shows an excess of  $160\mu\text{m}$  sources without redshifts having high  $S160/S70$  ratios ( $\text{Log}[S160/S70] \gtrsim 0.8$ ). These results may suggest that the excess sources are at high redshift ( $z \gtrsim 0.5$ ) and that the current redshift sample of  $160\mu\text{m}$  sources may be

biased toward lower redshifts.

### 4.3. Infrared Luminosity

For the  $70\mu\text{m}$  selected sources, we can estimate the average infrared luminosity for the xFLS population. The rest-frame wavelength of the MIPS-70 band corresponds to  $60\mu\text{m}$  at a redshift of  $z \simeq 0.2$ . The FIR luminosity ( $42.5\text{--}122.5\mu\text{m}$ ) can be derived from the rest-frame  $60\mu\text{m}$  and  $100\mu\text{m}$  flux densities (Helou, Soifer, & Rowan-Robinson 1985). By using the SED associated with the average model parameters of  $T_d \simeq 30\text{K}$  and  $\alpha \simeq 2.4$  for the xFLS sources, we estimate a rest-frame  $S100/S60 = 2 \pm 1$  observed for the bulk of the *IRAS* galaxies (Sanders et al. 2003). Based on the rest-frame  $S100/S60$  ratio, the corresponding FIR flux is  $\text{FIR}(\text{W m}^{-2}) = 6.1 \times 10^{-14} (S70/\text{Jy})$  for the observed  $S70$  flux density at  $z \simeq 0.2$ . For galaxies at  $z \simeq 0.2$ , the average value of  $S70$  is  $33\text{mJy}$ . This corresponds to a FIR luminosity of  $L(\text{FIR}) = 6.0 \times 10^{10} L_\odot$ . Using the models of Dale et al. (2001) and the estimated  $S100/S60$  ratio, the total infrared luminosity ( $3\text{--}1100\mu\text{m}$ )  $L(\text{TIR}) = 2.3L(\text{FIR})$ . Hence, the average total infrared luminosity of the  $70\mu\text{m}$ -selected xFLS galaxies at  $z \simeq 0.2$  is about  $L(\text{TIR}) = 1.4 \times 10^{11} L_\odot$ .

Although the redshift survey for the  $70\mu\text{m}$ -selected sources is not currently complete, the infrared luminosity function can be estimated at low redshift for bright flux densities. At  $S70 > 50\text{mJy}$ , 72% (65/90) of sources have redshifts. The majority of sources without redshifts are suspected to be at high redshift given that the observed redshift distribution declines significantly at  $z > 0.3$  and the models predict that the majority of sources at these flux density levels are at  $z > 0.3$ . Based on the models of Lagache et al. (2004), about 40–45% of galaxies with  $S70 > 50\text{mJy}$  are predicted to be at  $z < 0.3$ . Assuming  $\sim 100\%$  completeness at  $z < 0.3$  (i.e., assume all sources with  $S70 > 50\text{mJy}$  currently without redshifts are at  $z > 0.3$ ), we find  $64 \pm 9\%$  (58/90) of galaxies with  $S70 > 50\text{mJy}$  and  $z < 0.3$ . If the current xFLS redshift surveys are not complete at  $z < 0.3$  (with  $S70 > 50\text{mJy}$ ), then the models would be even more discrepant with the observations. Hence, the models may under predict the percentage of low redshift  $70\mu\text{m}$  sources at bright flux densities. There are two potential caveats on this result. First, a small percentage ( $< 1\%$ ) of  $70\mu\text{m}$  sources do not have  $24\mu\text{m}$  counterparts, and these sources are likely to be at high redshift (e.g., at  $z \sim 1.5$  where the silicate absorption feature is redshifted into the  $24\mu\text{m}$  band). However, there is only one  $70\mu\text{m}$  source without a  $24\mu\text{m}$  counterpart with  $S70 > 50\text{mJy}$ , so this population, by itself, cannot account for the apparent discrepancy with the models. The second caveat is that we have thrown out 9% of the  $70\mu\text{m}$  sources with multiple possible  $24\mu\text{m}$  matches (Sec. 4.2). The  $70\mu\text{m}$  sources with multiple candidate  $24\mu\text{m}$  counterparts tend to be brighter on average and typically have low redshifts. In fact, we find only one such source with  $z > 0.3$  and with  $S70 > 50\text{mJy}$  (1/70 with redshifts). Additional redshift surveys are needed to confirm the findings here which suggest that the current models slightly over predict the percentage of bright  $70\mu\text{m}$  sources ( $S70 > 50\text{mJy}$ ) at high-redshift ( $z > 0.3$ ) and their contribution to the total CIB.

To estimate the infrared luminosity function, we use the

sample of 58 galaxies with  $S70 > 50$  mJy and  $z < 0.3$ . We adopt the  $1/V_{max}$  method following the calculation of the *IRAS*  $\nu L_\nu(60\mu\text{m})$  luminosity function (Soifer et al. 1987). For each source, the maximum volume ( $V_{max}$ ) at which the source would be included in the sample is computed, using  $V_{max}(z = 0.3)$  as an upper bound for the survey. The  $70\mu\text{m}$  flux density is converted to a rest-frame  $60\mu\text{m}$  flux density using a power-law interpolation between the observed  $24\mu\text{m}$  and  $70\mu\text{m}$  measurements. The calculated xFLS  $60\mu\text{m}$  luminosity function ( $\rho$ ) shown in Figure 10 represents the space density of galaxies per  $\text{Mpc}^3$  per magnitude in luminosity. Even though the current xFLS sample is a factor of 100 deeper in flux density than the *IRAS*  $60\mu\text{m}$  bright galaxy sample (Soifer et al. 1987; Sanders et al. 2003), the xFLS sample does not yet probe the high luminosity end of the luminosity function ( $\text{Log}(\nu L_\nu[60\mu\text{m}]/L_\odot) > 11.5$ ), given the low redshift range (median redshift of only  $z = 0.096$ ) and small area of the current sample. The derived xFLS luminosity function agrees well with the *IRAS*  $60\mu\text{m}$  luminosity function (Soifer et al. 1987). Below  $\text{Log}(\nu L_\nu[60\mu\text{m}]/L_\odot) < 10.5$ ,  $\rho \propto (\nu L_\nu)^{-0.8}$  (Soifer et al. 1987), while at higher luminosities  $\rho \propto (\nu L_\nu)^{-2.2}$  (Sanders et al. 2003). Additional redshifts for the faint  $S70 \sim 10$  mJy sources are needed to constrain the evolution of the luminosity function out to  $z \sim 1$ .

#### 4.4. Infrared to Radio Correlation

In the local universe, galaxies over a wide range of luminosity and Hubble types follow the empirical IR/radio correlation (Helou et al. 1985; Condon 1992). Observations of *ISO* sources (Gruppioni et al. 2003) indicate that the mid-IR to radio relationship holds out to  $z \sim 0.6$ , and the data for the SCUBA sources suggest that the FIR to radio relationship may be applicable even at  $z \sim 2-3$  (e.g., Chapman et al. 2005). With *Spitzer* we can measure the IR/radio relationship out to  $z \sim 1$  by direct observations near the peak of the SED, instead of estimating the IR luminosity from the shorter mid-IR or longer sub-mm wavelengths. Appleton et al. (2004) presented the first estimate of the IR/radio relationship based on *Spitzer* data. Their results were based on the early analysis of the xFLS data. Here we present updated results using more sensitive  $70\mu\text{m}$  data.

The sample of 427 xFLS-70 sources with redshifts and with only one candidate  $24\mu\text{m}$  counterpart (Sec. 4.2) was matched to the  $4\sigma$  radio catalog (Condon et al. 2003). Within  $3''$ , 325 of these xFLS-70 sources (76%) have radio counterparts. Figure 11 shows the observed  $S70/S(20\text{cm})$  ratio as a function of redshift for the matched galaxies.

At low redshift, the FIR to radio  $q$ -parameter is defined as  $q \equiv \text{Log}(FIR/(3.75 \times 10^{12} \text{W m}^{-2})) - \text{Log}(S(20\text{cm})/(\text{W m}^{-2}\text{Hz}^{-1})) = 2.3 \pm 0.2$  (Helou et al. 1985). Based on the typical SED of the xFLS sample of galaxies (Sec. 4.2), the corresponding predicted  $q$  parameter for the  $70\mu\text{m}$  to radio flux density ratio is  $q_{70} \equiv \text{Log}(S70/S[20\text{cm}]) = 2.09$  at  $z \simeq 0.2$ . We measure an average value of  $q_{70} = 2.10 \pm 0.16$  for xFLS galaxies at  $z \simeq 0.2$ . By comparison, Appleton et al. (2004) derived a similar value of  $q_{70} = 2.16 \pm 0.17$ , but unlike the previous results we observe the expected decrease of observed  $q_{70}$  as a function of redshift (Fig. 11). Based on the SEDs of local galaxies, we expect the observed  $q_{70}$  parameter to de-

crease with redshift since the average IR spectral index is significantly steeper than the radio spectral index. Assuming an IR spectral index of  $\alpha = 2.4$  based on the observed average ratio of  $S70/S24 = 14$  and the typical non-thermal radio spectral index of  $\alpha = 0.8$  ( $f_\nu \propto \nu^{-\alpha}$ , Condon et al. 1992), we expect  $q_{70} \propto (1+z)^{-1.6}$ . From a least-squares fit to the data, we estimate  $q_{70} \propto (1+z)^{-1.4 \pm 0.6}$ . Hence, the observed  $q_{70}$  for the xFLS galaxies follows the expected trend out to at least  $z \sim 1$  (Fig. 11).

## 5. CONCLUSIONS

The *Spitzer*  $70\mu\text{m}$  and  $160\mu\text{m}$  observations of the xFLS are presented. For the deeper verification field data, we measure number counts down to 8 mJy and 50 mJy ( $5\sigma$ ) in the  $70\mu\text{m}$  and  $160\mu\text{m}$  bands, respectively. The observed xFLS counts are consistent with previous measurements (Dole et al. 2004a) and are consistent within the uncertainties with the evolutionary models (Lagache et al. 2004). Based on the models of Lagache et al. (2004), approximately 35% of the CIB is resolved at  $70\mu\text{m}$  and 15% is resolved at  $160\mu\text{m}$  at the depth of the verification data. The observed fraction of low redshift galaxies at bright  $70\mu\text{m}$  flux densities is larger than model predictions and the total counts appear slightly systematically lower. These results may suggest the models overestimate the contribution of high-redshift galaxies at bright  $70\mu\text{m}$  flux densities to the total CIB. Deeper  $70\mu\text{m}$  observations are needed for measuring the expected turn over in the differential source counts to provide better constraints on the evolutionary models.

The observed xFLS infrared colors  $S70/S24$  and  $S160/S70$  are consistent with the results from the *IRAS* and *ISO* missions. Modeled SED fits suggest an average  $160\mu\text{m}/70\mu\text{m}$  color temperature for the dust of  $T_d \simeq 30$  K, for the  $160\mu\text{m}$ -selected sample of galaxies. This temperature is consistent with *ISO* observations of spirals (Bendo et al. 2003). The average  $S70/S24$  ratio implies an infrared spectral index of  $\alpha \simeq 2.4$ , which agrees with expectations from the average *IRAS*  $S60/S24$  ratio (Soifer et al. 1989; Sanders et al. 2003). The observed  $70\mu\text{m}$  infrared to radio correlation of the xFLS sources also agrees well with the FIR-to-radio correlation found for local star-forming galaxies (Helou et al. 1985; Condon et al. 1992). We observe a trend of decreasing  $S70/S(20\text{cm})$  as a function of redshift consistent with expectations based on the SEDs of local galaxies.

Given the lack of sufficient redshift measurements for the high-redshift faint xFLS-Ge sources, we can only derive an infrared luminosity function at low redshift for only the brightest  $70\mu\text{m}$  galaxies. With these data, we calculate a rest-frame  $60\mu\text{m}$  luminosity function for the xFLS that agrees well with the *IRAS* luminosity function (Soifer et al. 1987). In the future, it may be possible to measure the evolution of the luminosity function out to moderate redshifts with the xFLS data when additional redshift surveys of faint  $70\mu\text{m}$  sources become available.

We thank all of our colleagues associated with the *Spitzer* mission who have made these observations possible. This work is based on observations made with the *Spitzer Space Telescope*, which is operated by the Jet Propulsion Laboratory, California Institute of Technology under NASA contract 1407.

## REFERENCES

- Appleton, P. N., et al. 2004, *ApJS*, 154, 147  
 Armus, L., et al. 2004, *ApJS*, 154, 178  
 Beichman, C. A., Neugebauer, G., Habing, H. J., Clegg, P. E., & Chester, T. J. 1988, *Infrared Astronomical Satellite (IRAS) Catalogs and Atlases. Volume 1: Explanatory Supplement* (Washington, DC: US Government Printing Office)  
 Bendo, G. J., et al. 2003, *AJ*, 125, 2361  
 Blain, A. W., Barnard, V. E., & Chapman, S. C. 2003, *MNRAS*, 338, 733  
 Blain, A. W., Smail, I., Ivison, R. J., Kneib, J.-P., & Frayer, D. T. 2002, *Physics Reports*, 369, 111  
 Chapman, S. C., Blain, A. W., Smail, I., & Ivison, R. J. 2005, *ApJ*, 622, 772  
 Chary, R., et al. 2004, *ApJS*, 154, 80  
 Chary, R., & Elbaz, D. 2001, *ApJ*, 556, 562  
 Condon, J. J. 1992, *ARA&A*, 30, 575  
 Condon, J. J., Cotton, W. E., Yin, Q. F., Shupe, D. L., Storrie-Lombardi, L. J., Helou, G., Soifer, B. T., & Werner, M. W. 2003, *AJ*, 125, 2411  
 Dale, D. A., & Helou, G. 2002, *ApJ*, 576, 159  
 Dale, D. A., Helou, G., Contursi, A., Silbermann, N. A., & Kolhatkar, S. 2001, *ApJ*, 549, 215  
 Diolaiti, E., Bendinelli, O., Bonaccini, D., Close, L., Currie, D., & Parmeggiani, G. 2000, *A&AS*, 147, 335  
 Dole, H., et al. 2004a, *ApJS*, 154, 87  
 Dole, H., et al. 2004b, *ApJS*, 154, 93  
 Dunne, L., Eales, S., Edmunds, M., Ivison, R., Alexander, P., & Clements, D. L. 2000, *MNRAS*, 315, 115  
 Elbaz, D., Cesarsky, C. J., Chantal, P., Aussel, H., Franceschini, A., Fadda, D., & Chary, R. R. 2002, *A&A* 384, 848  
 Elbaz, D. et al. 1999, *A&A*, 351, L37  
 Fadda, D., Jannuzi, B. T., Ford, A., & Storrie-Lombardi, L., J. 2004, *AJ*, 128, 1  
 Gordon, K. D., et al. 2005, *PASP*, 117, 503  
 Gruppioni, C., Pozzi, F., Zamorani, G., Ciliegi, P., Lari, C., Calabrese, E., La Franca, F., & Matute, I. 2003, *MNRAS*, 341, L1  
 Hauser, M. G., & Dwek, E. 2001, *ARA&A*, 39, 249  
 Helou, G., Soifer, B. T., & Rowan-Robinson, M. 1985, *ApJ*, 298, L7  
 Hesselroth, T., Ha, E. C., Pesenson, M., Kelly, D. M., Rivlis, G., & Engelbracht, C. W. 2000, *Spaceborne Infrared Remote Sensing VIII, SPIE Conference Proceedings*, 4131, 26  
 King, A. J., & Rowan-Robinson, M. 2003, *MNRAS*, 339, 260  
 Lagache, G., et al. 2004, *ApJS*, 154, 112  
 Lonsdale, C. J., et al. 2004, *ApJS*, 154, 54  
 Lortet, M.-C., Borde, S., & Ochsenbein, F. 1994, *A&AS*, 107, 193  
 Makovoz, D., & Marleau, F. R. 2005, *PASP*, in press  
 Marleau, F. R., et al. 2004, *ApJS*, 154, 66  
 Miley, G. K., Neugebauer, G., & Soifer, G. T. 1985, *ApJ*, 293, L11  
 Neugebauer, G., et al. 1984, *ApJ*, 278, L1  
 Papovich, C., et al. 2004, *ApJS*, 154, 70  
 Rieke, G. H., et al. 2004, *ApJS*, 154, 25  
 Rodighiero, G., Fadda, D., Franceschini, A., & Lari, C. 2005, *MNRAS*, 357, 449  
 Sanders, D. B., Mazzarella, J. M., Kim, D.-C., Surace, J. A., & Soifer, B. T. 2003, *AJ*, 126, 1607  
 Soifer, B. T., Boehmer, G., Neugebauer, G., & Sanders, D. B. 1989, *AJ*, 98, 766  
 Soifer, B. T., Sanders, D. B., Madore, B. F., Neugebauer, G., Danielson, G. E., Elias, J. H., Lonsdale, C. J., & Rice, W. L. 1987, *ApJ*, 320, 238  
 Spoon, H. W. W., et al. 2004, *ApJS*, 154, 184  
 Strauss, M. A., et al. 2002, *AJ*, 124, 1810  
 Werner, M. W., et al. 2004, *ApJS*, 154, 1  
 Xu, C., Lonsdale, C. J., Shupe, D. L., O'Linger, J., & Masci, F. 2001, *ApJ*, 562, 179

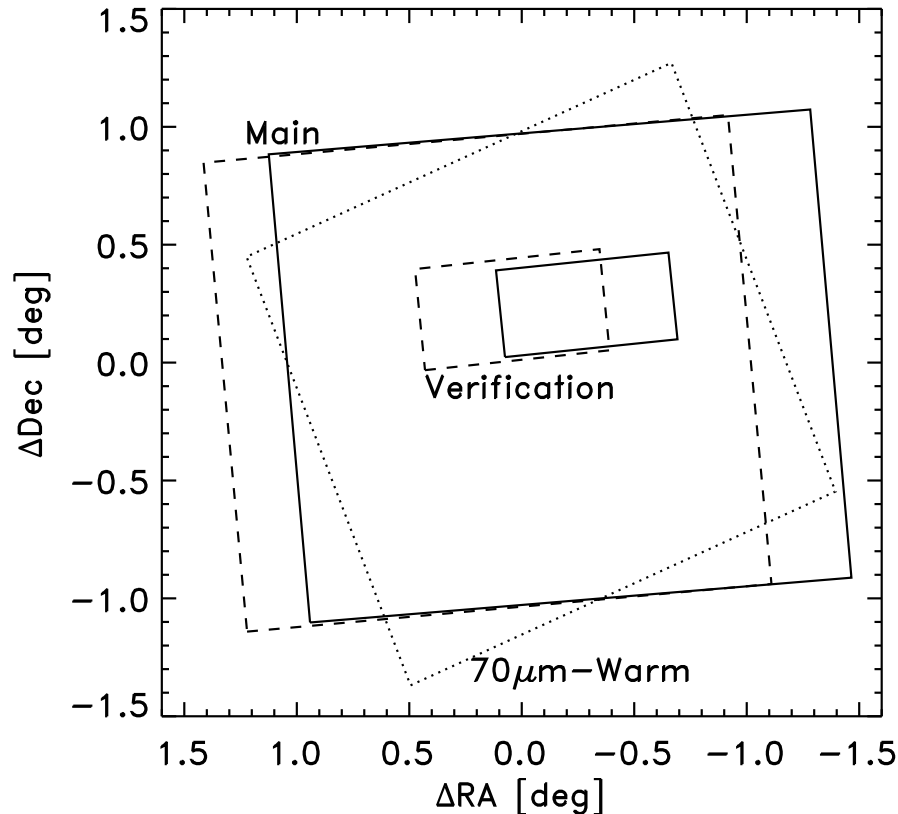


FIG. 1.— The layout of the  $70\mu\text{m}$  and  $160\mu\text{m}$  fields for the xFSL observations. The  $70\mu\text{m}$  main and verification fields are shown by the solid-lines, while the  $160\mu\text{m}$  xFSL fields are shown as dashed-lines. The location of the  $70\mu\text{m}$ -warm observations taken in 2005 May is shown by the dotted-line. The right ascension and declination offsets are with respect to the center of the main field ( $17^{\text{h}}18^{\text{m}}00^{\text{s}}$ ,  $+59^{\circ}30'00''$ ).



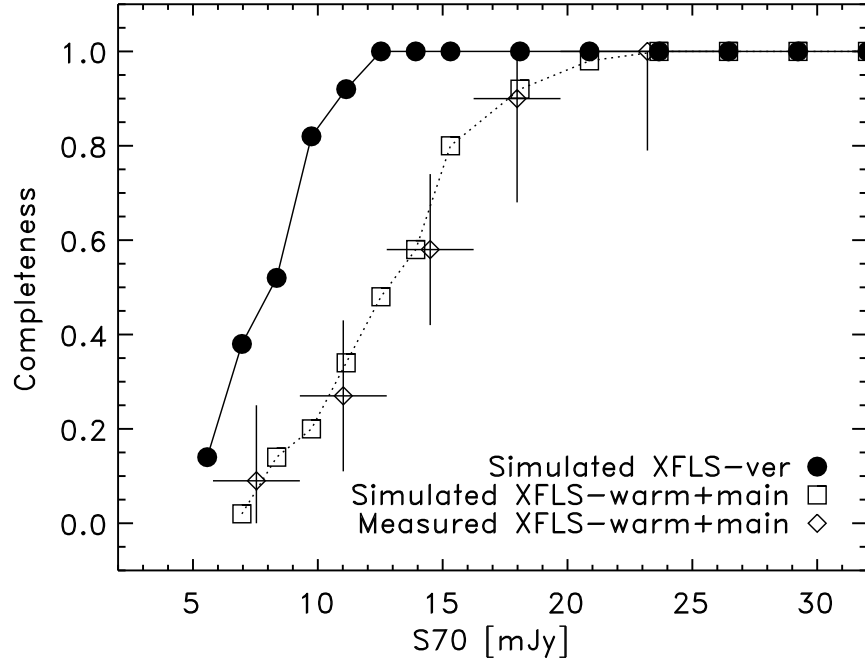


FIG. 2.— The  $70\mu\text{m}$  completeness level as a function of flux density for the verification and warm+main xFLS surveys. The diamonds represent empirical measurements of the warm+main survey based on the deeper verification data, and the squares and solid circles are the results of simulations for the warm+main and verification fields respectively. The completeness estimates are for the  $S/N > 5$  source lists used to derive the counts.

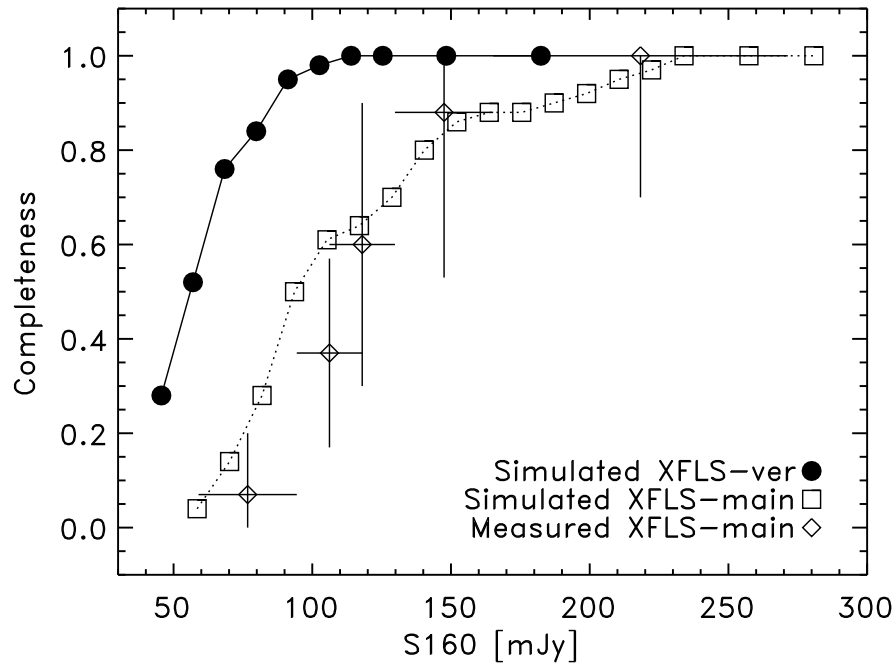


FIG. 3.— The  $160\mu\text{m}$  completeness level as a function of flux density for the verification and main xFLS surveys. The diamonds represent empirical measurements of the main survey based on the deeper verification data, and the squares and solid circles are the results of simulations for the main and verification fields respectively. The completeness estimates are for the  $S/N > 5$  source lists used to derive the counts.

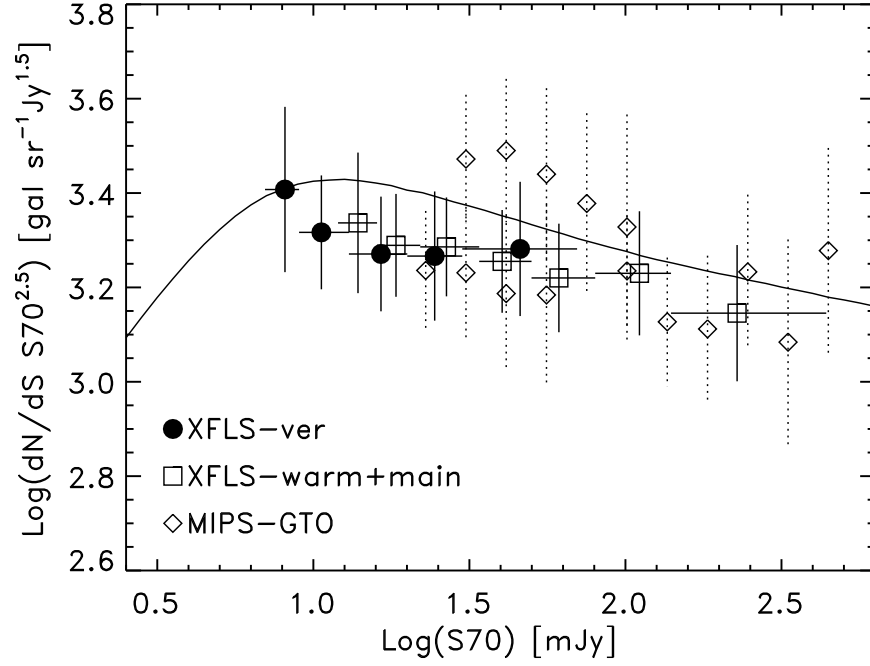


FIG. 4.— The  $70\mu\text{m}$  differential number counts for the verification (solid circles) and warm+main (squares) xFLS surveys. The diamonds represent previous MIPS-GTO measurements (Dole et al. 2004a). The vertical error bars include the uncertainties of the absolute flux density scale and completeness, and the horizontal line segments show the bin sizes. The solid line is the evolutionary model of Lagache et al. (2004).

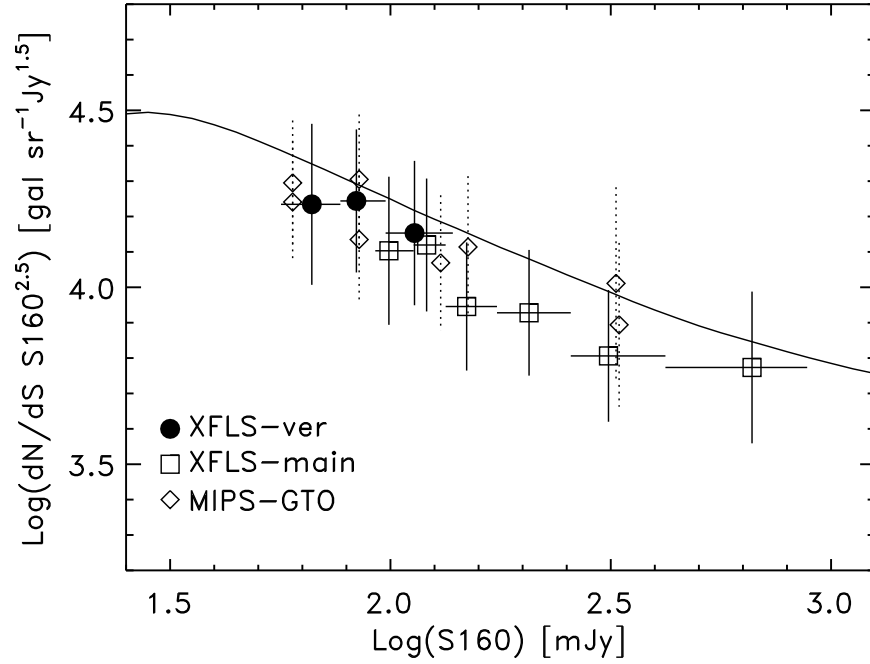


FIG. 5.— The  $160\mu\text{m}$  differential number counts for the verification (solid circles) and main (squares) xFLS surveys. The diamonds represent previous MIPS-GTO measurements (Dole et al. 2004a). The vertical error bars include the uncertainties of the absolute flux density calibration scale and completeness, and the horizontal line segments show the bin sizes. The solid line is the evolutionary model of Lagache et al. (2004).

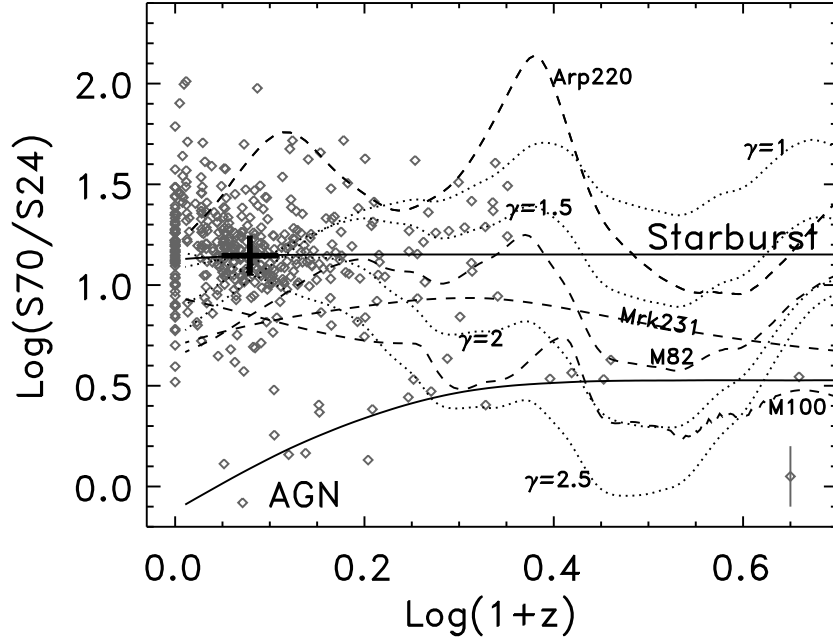


FIG. 6.— The S70/S24 flux density ratio for  $70\mu\text{m}$  sources with redshifts. The ULIRGs Arp 220 and Mrk 231, the starburst M82, and the spiral galaxy M100 are shown as dashed lines. The solid lines represent simple modified blackbody SED models for starbursts ( $\alpha = 2.4$ ,  $T_d = 30\text{ K}$ ) and AGN ( $\alpha = 1.1$ ,  $T_d = 90\text{ K}$ ). The dotted lines show the SED models of Dale & Helou (2002) as a function of  $\gamma$ , where  $\gamma \sim 2$ – $2.5$  represent more quiescent star-forming galaxies and  $\gamma \sim 1.5$ – $1$  represent more active galaxies. The plus symbol shows the predicted S70/S24 ratio at a redshift  $z = 0.2$  based on the average *IRAS* S60/S25 ratio. The typical error bar for the data points from the  $4\sigma$  source lists is shown in the lower right.

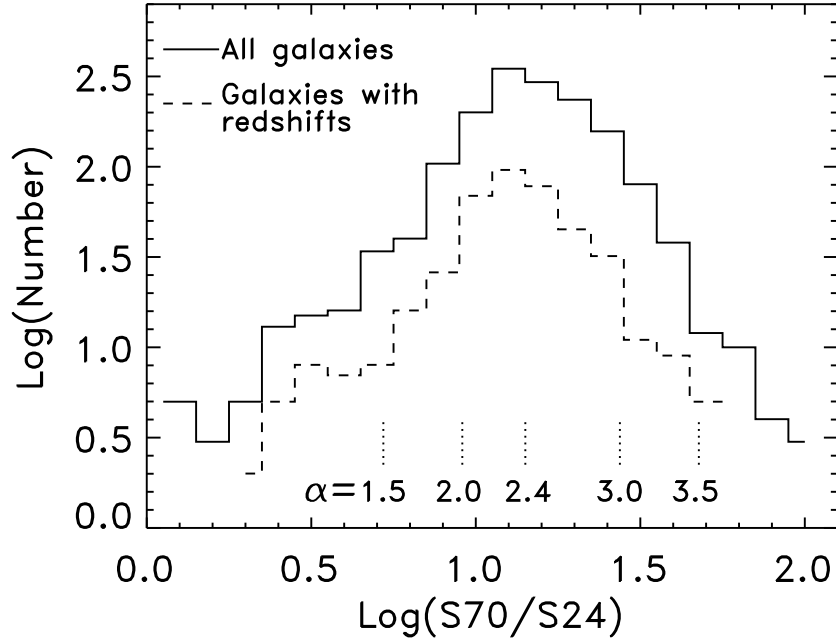


FIG. 7.— The distributions of the S70/S24 flux density ratios for  $70\mu\text{m}$  sources with redshifts shown in Fig. 6 (dashed line) and for all  $70\mu\text{m}$ -selected sources (solid line). Values for a range of infrared spectral indexes ( $\alpha$ ) are shown by the vertical dotted lines.

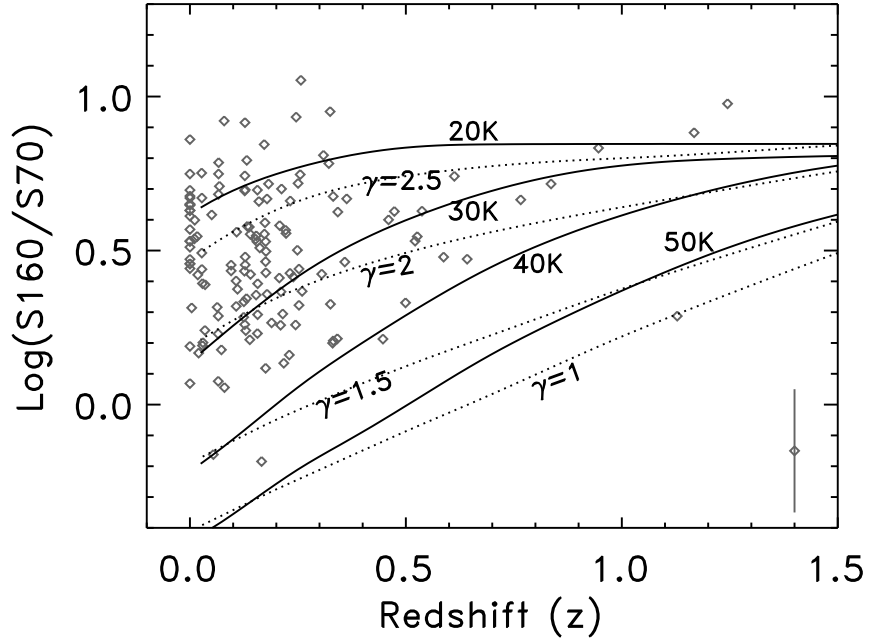


FIG. 8.— The S160/S70 flux density ratio for  $160\mu\text{m}$ -selected sources with redshifts. The solid lines show simple modified blackbody SED models based on different dust temperatures (20–50 K) assuming an infrared spectral index of  $\alpha = 2.4$  and a dust emissivity index of  $\beta = 1.5$ . The dotted lines show the SED models of Dale & Helou (2002) as a function of  $\gamma$ . The typical error bar for the data points from the  $4\sigma$  source lists is shown in the lower right.

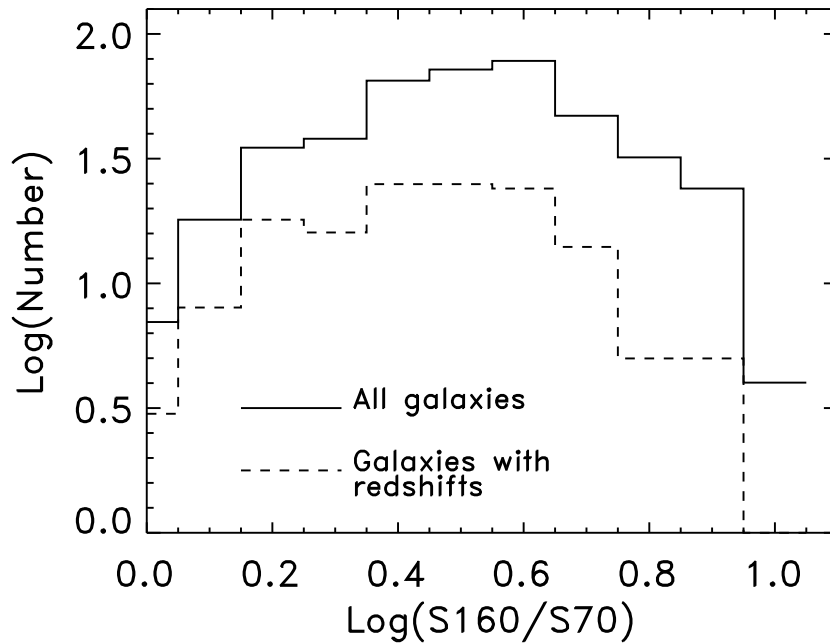


FIG. 9.— The distributions of the S160/S70 flux density ratios for the  $160\mu\text{m}$  sources with redshifts shown in Fig. 8 (dashed line) and for all  $160\mu\text{m}$ -selected sources (solid line). The excess of sources without redshifts at the higher S160/S70 ratios may suggest that the current redshift sample of  $160\mu\text{m}$  sources is biased toward lower redshifts.

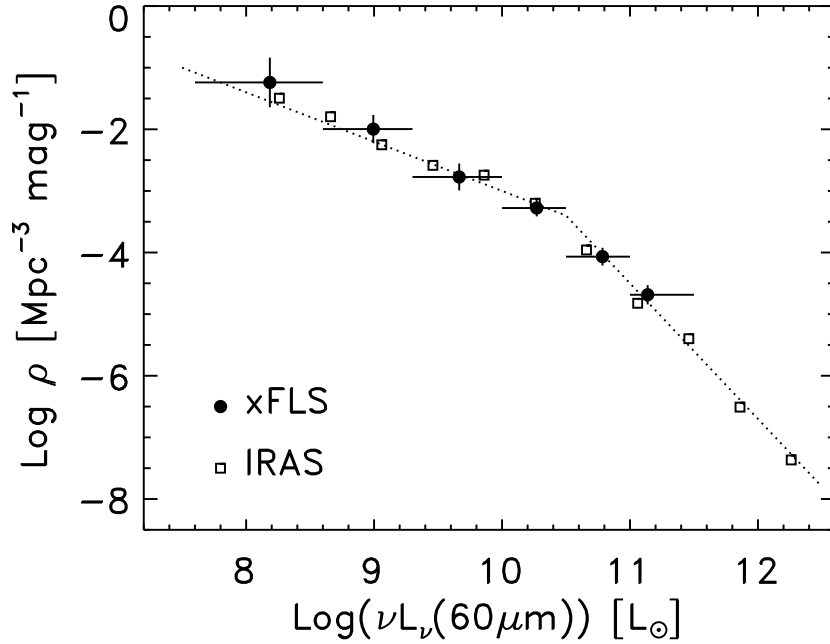


FIG. 10.— The xFLS rest-frame  $60\mu\text{m}$  luminosity function based on the sources with  $S_{70} > 50 \text{ mJy}$  and  $z < 0.3$  (solid circles). The *IRAS*  $60\mu\text{m}$  luminosity function is represented by the squares (Soifer et al. 1987), corrected for the adopted value of  $H_0 = 70 \text{ km s}^{-1} \text{ Mpc}^{-1}$ . The dotted-line shows the double power-law fit of the luminosity function based on the *IRAS* data (Soifer et al. 1987; Sanders et al. 2003).

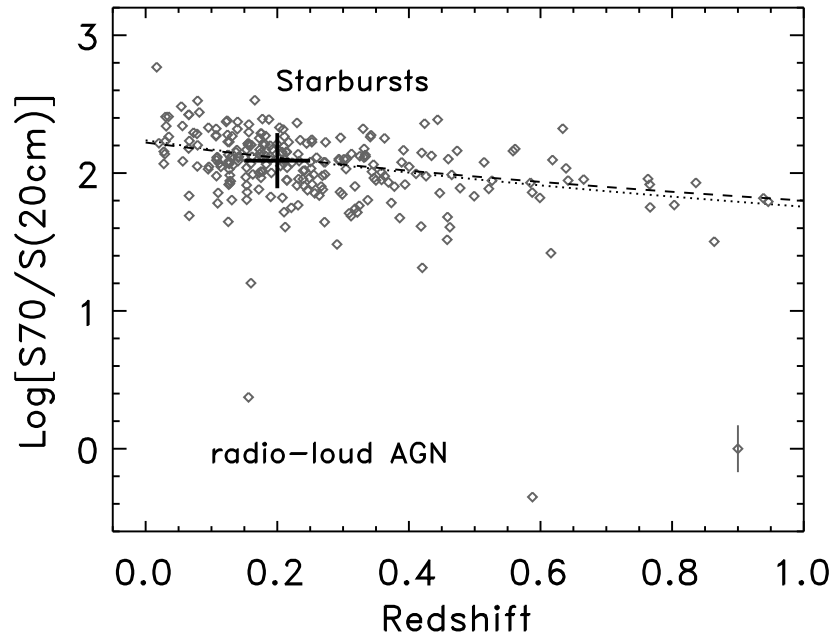


FIG. 11.— The  $S_{70}/S(20 \text{ cm})$  flux density ratio for the  $70\mu\text{m}$ -selected xFLS sources with redshifts between  $0 < z < 1$ . The dotted-line shows the expected behavior of  $S_{70}/S(20 \text{ cm}) \propto (1+z)^{-1.6}$ , assuming power-law approximations for the SEDs at radio and infrared wavelengths. The dashed-line shows the result of a least-squares fit [ $S_{70}/S(20 \text{ cm}) \propto (1+z)^{-1.4 \pm 0.6}$ ]. The plus symbol shows the predicted value of the  $S_{70}/S(20 \text{ cm})$  ratio based on the local infrared to radio correlation. The typical error bar for the data points from the  $4\sigma$  source lists is shown in the lower right.

TABLE 1  
*Spitzer* EXTRAGALACTIC FLS MIPS-GE OBSERVATIONS

Field	$t_{int}$ (s)		$5\sigma$ (mJy)		Area (deg <sup>2</sup> )
	70 $\mu$ m	160 $\mu$ m	70 $\mu$ m	160 $\mu$ m	
Main . . . . .	42	8	19	100	4.5
Verification .	252	42	8	50	0.35
Warm+Main	84	. . . . .	14	. . . . .	3.3

NOTE.—The integration time ( $t_{int}$ ) is the average integration time for the field. The approximate average  $5\sigma$  noise levels are for point sources and do not include the absolute flux density calibration uncertainties.

TABLE 2  
 EXTRAGALACTIC FLS 70 $\mu$ m CATALOG

Source Name	$\alpha$ (J2000) (deg)	$\delta$ (J2000) (deg)	Error (arcsec)	S70 (mJy)	Flag
(1)	(2)	(3)	(4)	(5)	(6)
FLS70 J172723.3+601626	261.84712	60.27414	1.9	81.4 $\pm$ 12.9	prf
FLS70 J172716.2+600051	261.81791	60.01433	1.6	1610.1 $\pm$ 244.6	a120m
FLS70 J172709.5+600141	261.78960	60.02815	2.1	77.3 $\pm$ 12.7	prf
FLS70 J172704.7+593736	261.76978	59.62680	2.0	62.1 $\pm$ 9.9	prf
FLS70 J172651.1+601851	261.71329	60.31419	3.3	34.7 $\pm$ 7.0	prf

NOTE.—The entire xFLS 70 $\mu$ m catalog ( $> 7\sigma$ ) is presented in the electronic edition of the *Astronomical Journal*. A portion of Table 2 is shown here for guidance regarding the form and content of the catalog. Column (1) gives the source name following the IAU designations (Lortet, Borde, & Ochsenbein 1994). Column (2) and column (3) are the right ascension ( $\alpha$ ) and declination ( $\delta$ ) J2000.0 source positions in decimal degrees. Column (4) provides the radial positional uncertainty in arcsec ( $1\sigma$ ). Column (5) gives the flux density measurement in mJy. The flux density errors include the uncertainties of the absolute flux density scale. Column (6) provides a flag for the flux density measurement method. A flag of “prf” indicates that the source was fitted by the PRF, while a flag starting with an “a” indicates that an aperture measurement was used (for cases of extended sources and/or close blends). The number following the “a” gives the aperture diameter in arcsec; e.g., a120 implies an aperture diameter of 120”. Sources with aperture flags ending with a “m” represent bright galaxies not well fitted by the PRF and with nearby companions; in these cases, the flux density of the bright galaxy was derived by subtracting the PRF measurement(s) of the nearby faint point source(s) from the total aperture flux density.

TABLE 3  
EXTRAGALACTIC FLS  $160\mu m$  CATALOG

Source Name (1)	$\alpha$ (J2000) (deg) (2)	$\delta$ (J2000) (deg) (3)	Error (arcsec) (4)	S160 (mJy) (5)	Flag (6)
FLS160 J172902.1+600523	262.25801	60.08859	3.4	294.8 $\pm$ 76.0	prf
FLS160 J172855.5+600026	262.23039	60.00619	7.4	154.4 $\pm$ 44.2	prf
FLS160 J172851.3+600821	262.21295	60.13807	3.8	293.7 $\pm$ 76.4	prf
FLS160 J172826.5+600539	262.10963	60.09320	3.0	1211.0 $\pm$ 310.5	a192
FLS160 J172817.7+600100	262.07271	60.01573	5.9	188.4 $\pm$ 50.97	prf

NOTE.—The entire xFLS  $160\mu m$  catalog ( $> 7\sigma$ ) is presented in the electronic edition of the *Astronomical Journal*. A portion of Table 3 is shown here for guidance regarding the form and content of the catalog. Column headers are the same as described in Table 2.

TABLE 4  
EXTRAGALACTIC FLS  $70\mu m$  NUMBER COUNTS

Average $S_\nu$ (mJy)	$S_{\text{low}}$ (mJy)	$S_{\text{high}}$ (mJy)	Number	Completeness	$dN/dS S^{2.5}$ (gal sr $^{-1}$ Jy $^{1.5}$ )
8.1	7	9	46	0.50 $\pm$ 0.15	2556 $\pm$ 1030
10.6	9	13	61	0.80 $\pm$ 0.08	2073 $\pm$ 575
16.5	13	20	40	1.0 $\pm$ 0.05	1866 $\pm$ 522
24.5	20	30	21	1.0 $\pm$ 0.03	1847 $\pm$ 582
46.0	30	70	18	1.0 $\pm$ 0.03	1912 $\pm$ 626
13.9	12	16	230	0.60 $\pm$ 0.15	2172 $\pm$ 744
18.4	16	22	230	0.90 $\pm$ 0.08	1883 $\pm$ 453
26.7	22	34	200	1.00 $\pm$ 0.05	1931 $\pm$ 466
40.3	34	50	89	1.00 $\pm$ 0.03	1800 $\pm$ 451
61.2	50	80	54	1.00 $\pm$ 0.03	1660 $\pm$ 439
110.9	80	140	25	1.00 $\pm$ 0.03	1698 $\pm$ 514
227.9	140	440	17	1.00 $\pm$ 0.03	1398 $\pm$ 464

NOTE.—The first five entries are the  $70\mu m$  counts for the verification field, while the remaining entries are for the warm+main  $70\mu m$  survey. The uncertainties for the differential counts ( $dN/dS S^{2.5}$ ) include the Poisson noise, the completeness uncertainty, and the absolute flux density calibration uncertainty of 15%. The counts are based on the  $> 5\sigma$  source lists, corrected for completeness.

TABLE 5  
EXTRAGALACTIC FLS  $160\mu\text{m}$  NUMBER COUNTS

Average $S_\nu$ (mJy)	$S_{\text{low}}$ (mJy)	$S_{\text{high}}$ (mJy)	Number	Completeness	$dN/dS S^{2.5}$ (gal sr $^{-1}$ Jy $^{1.5}$ )
68.0	56.4	77.0	17	0.55 $\pm$ 0.15	17156 $\pm$ 8978
85.9	77.0	97.5	15	0.85 $\pm$ 0.08	17541 $\pm$ 8155
116.4	97.5	138.6	13	0.97 $\pm$ 0.05	14231 $\pm$ 6678
101.8	92.4	112.9	60	0.55 $\pm$ 0.15	12682 $\pm$ 6104
124.0	112.9	133.4	45	0.65 $\pm$ 0.1	13170 $\pm$ 5688
152.8	133.4	174.5	44	0.80 $\pm$ 0.08	8825 $\pm$ 3674
211.7	174.5	256.6	43	0.92 $\pm$ 0.05	8472 $\pm$ 3460
320.7	256.6	420.8	25	1.0 $\pm$ 0.05	6399 $\pm$ 2738
679.0	420.8	882.6	10	1.0 $\pm$ 0.05	5935 $\pm$ 2926

NOTE.—The first three entries are the  $160\mu\text{m}$  counts for the verification field, while the remaining entries are for the main  $160\mu\text{m}$  survey. The uncertainties for the differential counts ( $dN/dS S^{2.5}$ ) include the Poisson noise, the completeness uncertainty, and the absolute flux density calibration uncertainty of 25%. The counts are based on the  $> 5\sigma$  source lists, corrected for completeness.